Transport Properties of Few-Layer NbSe₂: from Electronic Structure to Thermoelectric Properties

Tianhui Zhu¹, Peter M. Litwin², Md. Golam Rosul¹, Devin Jessup², Md. Sabbir Akhanda¹, Farjana F. Tonni¹, Sergiy Krylyuk³, Albert V. Davydov³, Petra Reinke^{2,4}, Stephen J. McDonnell^{2,4} and Mona Zebarjadi^{1,2,4}

Abstract

4-layer NbSe₂ is grown on SiO₂ by molecular beam epitaxy. The in-situ X-ray photoelectron spectroscopy measurements suggest an Nb-rich stoichiometry (Nb_{1+x}Se₂) likely due to the intercalation of Nb atoms in between the NbSe₂ layers. The metallic nature of the samples is confirmed using scanning tunneling microscopy and local density of state measurements as well as band structure calculations. This metallic nature is consistent with the small measured Seebeck coefficient and large electrical conductivity values. A change of sign in the Seebeck coefficient is observed in the bulk single crystal sample at 50 K, and in the polycrystalline few-layer sample at 120 K. Since the samples are metallic, this change of sign is the result of a change in the density of state slope at the Fermi level. The temperature dependence of the measured Seebeck coefficient matches with theoretical calculations for 4 layer NbSe₂. The room temperature Seebeck coefficient is negative, but when oxidized, that of the few-layer sample changed to positive. The in-plane thermal conductivity of the few-layer samples is measured using the heat diffusion imaging method at low temperatures and is (32 ± 10) W/m·K at 200 K.

Keywords: two-dimensional materials, molecular beam epitaxy, niobium selenide, thermoelectric, density functional theory, scanning tunneling microscopy

1. Introduction

Two-dimensional (2D) materials possess a wide range of electronic properties, from insulating to superconducting, depending on their crystalline structures and the topology of their electronic structure. These properties can be tuned by mechanical strain [1,2], applied field [3], and the number of

layers [4,5]. Transition metal dichalcogenides (TMDs), as an important family of 2D materials, share most of these traits [6]. In terms of thermoelectric applications, 2D confined states can result in a large Seebeck coefficient: many few-layer samples have shown superior thermoelectric properties compared to their equivalent bulk counterparts, and hence are of interest for thermoelectric energy conversion [7] and

¹ Department of Electrical and Computer Engineering, University of Virginia, Charlottesville, VA, 22904, United States

² Department of Materials Science and Engineering, University of Virginia, Charlottesville, VA, 22904, United States

³ Materials Science and Engineering Division, National Institute of Standards and Technology, Gaithersburg, MD, 20899, United States

⁴ Authors to whom any correspondence should be addressed, <u>pr6e@virginia.edu</u> (P.R.), <u>sjm3qf@virginia.edu</u> (S.J.M.) and <u>m.zebarjadi@virginia.edu</u> (M.Z.).

nanoscale cooling applications [8]. For instance, at room temperature, monolayer graphene/hBN has a power factor times temperature (*PFT*) of about 10 W/m·K [9], which is an order of magnitude larger than a commercial bulk Bi₂Te₃. The best-performing low-temperature TMD sample to date is MoS₂/hBN with a *PFT* of about 1.5 W/m·K at 30 K [10], which is larger than most bulk samples at a similar temperature.

Among TMDs, NbSe₂ is of particular interest. In its 2H phase, charge density waves (CDWs) and superconductivity occur and coexist at low temperatures (below 7 K for bulk crystals), with the superconducting state and the CDW transition temperature depending on thickness [11-13]. 2H-NbSe₂ has been studied extensively as an exemplary system for highly correlated electronic states both experimentally and theoretically [11–15]. Its electrical and magneto-transport properties have been used at low temperatures to identify the superconducting or the CDW phase of the sample [11,12,16]. It has been found that when an in-plane magnetic field is applied to a few-layer NbSe2, it exhibits two-fold rotational symmetry in the superconducting state as opposed to the threefold lattice symmetry [17]. Due to its non-centrosymmetric superconductivity, few-layer NbSe₂ can be fabricated into superconducting antenna devices, which have shown a reversible nonreciprocal sensitivity to electromagnetic waves with a wide range of frequencies [18].

In recent years, it was discovered that islands of the 1T polymorph of NbSe₂, which is thermodynamically unfavorable as a bulk material [19–22], could be grown by molecular beam epitaxy (MBE) [23]. Monolayer 1T-NbSe₂ is believed to be a Mott insulator in its CDW state according to several scanning tunneling microscopy (STM) studies [23–25]; while one study finds it to be a charge-transfer insulator [26]. Although not a focus of this study, this stable 1T phase in the few-layer limit has sparked renewed interest in NbSe₂ and adds to its application potential.

In this paper, we conduct a study on a few-layer Nb_{1+x}Se₂ grown by MBE on SiO₂/Si substrates. A single crystal bulk 2H-NbSe₂ sample grown by chemical vapor transport (CVT) was used as a reference. The MBE-grown material was characterized by X-ray photoelectron spectroscopy (XPS) and STM. In-plane thermoelectric transport measurements of the thin film samples, including normalized electrical resistance, electrical conductivity, and Seebeck coefficient were performed over a broad temperature range and compared with the bulk sample. The understanding of the transport properties was aided by first-principles calculations as well as STM probing. Finally, the in-plane thermal conductivity of fewlayer NbSe2 was measured using heat diffusion imaging, an electrical-pump optical-probe method based on the thermoreflectance technique, at low temperatures (50 K to 200 K). The thermal conductivity shows a maximum of 53 W/m·K at 120 K. Despite the relatively large electrical

conductivity values, using Wiedemann Franz law, we can estimate that the electronic contribution to the thermal conductivity is much smaller than the lattice contribution and the large thermal conductivity is from phonon conduction.

2. Material and Methods

2.1. Few-layer sample synthesis and XPS characterization

4-layer (4L) NbSe₂ was grown on SiO₂ by MBE. The SiO₂ substrate preparation varied depending on the nature of the oxide. 285 µm thick SiO₂/highly p-doped Si films were rinsed in acetone and isopropanol and blown dry with N₂ gas. The few-nm thick chemically grown SiO2/intrinsic Si layer was grown by first removing the native oxide using a 1% HF dip for 2 min. The SiO₂ layer was then produced by a 2-min. dip in a Piranha etch followed by a rinse in DI water and blown dry with N₂ gas. The samples were held to Mo sample plates using stripes of Ta foil which were spot welded to the sample plates. All samples were exposed to a 5-min. UV-O₃ treatment just before being introduced into the vacuum to remove any adsorbed contaminates. Once in ultra-high vacuum, the substrates were first held at 245 °C for 12 h. Then, prior to growth, the substrate was heated to 800 °C and held there for 10 min. to remove any physiosorbed species from the substrate. The substrate was then cooled down to the growth temperature of 770 °C. Se (99.999% pellets, Kurt J. Lesker) was evaporated from a standard effusion cell and Nb (99.9%, rod, Goodfellow Cambridge Ltd.) from a Focus EFM-4 ultra high vacuum (UHV) e-beam evaporator. The Nb rod was evaporated using a constant heating power (constant emission current and voltage). The heating power of Nb was set to provide a beam equivalence pressure of 2 × 10⁻⁹ mBar as determined by a beam flux monitor placed in the path of the Nb beam prior to growth. The beam pressure of Se was measured in the same way and ranged from 3.1×10^{-6} to 3.3×10^{-6} 10⁻⁶ mBar for samples grown in this work which resulted in flux ratios of ~1500:1. The growth of NbSe₂ was carried out by co-depositing the Nb and Se elemental sources continuously until the 4-layer films were completed. The thickness was estimated by reflection high energy electron diffraction (RHEED) and confirmed using in-situ XPS. At the end of the growth, the Nb source was closed, and the films were held at the growth temperature for 2 min. in a Se flux before turning off the sample heater and allowing the sample to cool in an Se flux for 10 min. The Se shutter was then closed to avoid Se condensation on the grown thin films. In-situ XPS was carried out using a monochromated Al-kα source (1486.7 eV) at 50 eV pass energy to study the chemical nature of the films and measure the final film thickness which was based on the attenuation of the Si 2p core level of the substrate. Prior to removal from UHV, amorphous Se capping layers were deposited in the MBE module at room temperature. Further

details of the MBE tool and in-situ characterization techniques used can be found elsewhere [27].

2.2. CVT growth

Single-crystalline NbSe₂ flakes were grown using iodine-assisted CVT method. Stoichiometric amounts of Nb (99.9 %, Strem Chemicals) and Se (99.999 %, Strem Chemicals) powders with a total weight of ≈ 1 g were loaded in a quartz ampoule together with ≈ 90 mg (3.8 mg/cm³) of I₂ transport agent. The ampoule was sealed under vacuum and placed in a single-zone furnace with the temperature at the charge and growth zones being 825 °C and 700 °C, respectively. The growth duration was 140 h. Lattice parameters of 2H-NbSe₂ crystals, a = b = 3.445(3) Å and c = 12.548(2) Å, were determined from powder X-ray diffraction scans (Bruker D8) using Materials Data Inc (MDI) Jade 6.5 software (Livermore, CA 2015).

2.3. Device fabrication

Two batches of NbSe₂ samples were grown to satisfy the different measurement setup requirements. One batch was grown on 285 nm thick SiO₂/highly p-doped Si (samples S1 to S4). This substrate was chosen for optimal optical contrast. Samples S1-S4 were grown on the same piece of SiO₂ substrate, which was later diced for different measurements. Another batch of samples was on chemically grown SiO₂/intrinsic Si substrate (sample S5). The intrinsic Si substrate was required to eliminate the substrate's contribution to the Seebeck measurements as contacts are attached to the sides of the sample.

Devices S1-S4 were fabricated following the same procedures with photolithography: the full coverage thin film was first etched by CF₄ plasma (30W, 120 s) to a well-defined rectangular area, then the electrodes (5 nm Ti/50 nm Au) were deposited using e-beam evaporation (base pressure of 10⁻⁶ Torr, deposition rate of 0.4 Å/s for Ti and 2.0 Å/s for Au). A schematic of the device configuration is provided in SM, which includes one heater close to one end of the thin film, two thermometers on top of the ends of the film, and four side contacts.

Device S5 was fabricated to fit the measurement setup for Quantum Design VERSALAB Thermal Transport Option (TTO). A picture of the electrode configuration is provided in SM. A two-component silver-filled epoxy was used to attach the 0.5 mm wide gold-coated Cu wire contacts.

The CVT bulk device was also measured inside the VERSALAB setup using similar configuration. The thin NbSe₂ flake was mounted on a glass substrate as added support for the electrodes. A picture is provided in SM.

2.4. Electrical resistance measurement

Standard 4-point probe configuration was used for all electrical resistance measurements. Electrical currents were sent through the contacts at the two ends of the samples, and electrical voltages were measured by the two contacts on the side of the samples, between the current leads.

2.5. Seebeck coefficient measurement

For S1, up to 30 mA current was supplied to the resistive heater for the temperature gradient. Temperature and voltage responses at the two ends of the sample were recorded by the two thermometers. The temperature response was acquired in form of changes in the thermometer resistances, which were then calibrated by changing the sample stage temperatures from 295 K to 310 K in a separate measurement.

For S5, the temperature dependence of the Seebeck coefficient was measured in the one-heater two-thermometer configuration employing the single-mode measurement technique of the TTO mode. One end of the sample was connected to a resistive heater while the other end was connected to the coldfoot of the sample puck. Two Cernox sensors placed along the length of the sample were used to measure the voltage and temperature difference simultaneously. An uncertainty of about 5% is estimated.

2.6. Thermal conductivity measurement

In-plane thermal conductivity was measured following the heat diffusion imaging method [28]. A $60\times$ Nikon objective with numerical aperture = 0.7 was used with the thermoreflectance imaging setup from Microsanj LLC. LEDs of 530 nm and 470 nm wavelengths served as the light source. Electrical pulses of 5 ms duration, 30% duty cycle and 5 V to 10 V voltages were supplied during measurements. The temperature maps were taken at a delay time of 5 ms, which was the end of the pulse.

2.7. DFT calculation

We used first-principle based DFT calculations to obtain the theoretical results. The band structure and the density of states were calculated using the QUANTUM ESPRESSO package [29]. The exchange-correlation functional was treated with generalized gradient approximation (GGA) in the form of modified Perdew-Burke-Ernzerhof (PBEsol) [30] functional. The interaction between the valence and core electrons was described using the projector augmented wave (PAW) pseudopotentials [31]. We set the plane-wave kinetic energy cutoff at 60 Ry with a charge density of 480 Ry. The geometry relaxation calculations were performed as a result of the Born Oppenheimer approximation [32], where the lattice parameters and the atomic coordinates were determined by minimizing the energy function within the adopted numerical approximations using the Broyden-Fletcher-Goldfarb-Shanno (BFGS) algorithm [33]. The convergence threshold for energy was set to 10^{-12} in the self-consistent calculation. We included approximately 14 Å of vacuum between the periodic replicas to simulate the four layers of the NbSe₂ structure. The Seebeck coefficients were calculated using the BoltzTrap [34] package with the semi-classical Boltzmann transport method in the constant relaxation time [35] approximation.

2.8. STM measurement

The 4-layer NbSe₂ sample was examined using an Omicron Nanotechnology Variable Temperature Scanning Probe Microscopy system (VT-STM) with a base pressure of 5×10^{-10} mbar and the sample at ambient temperature. The topography images were acquired with an electrochemically etched tungsten tip and imaging conditions are marked in each image; the most frequently used imaging conditions were V_{bias} = 0.45 V and I_t = 0.2 nA, and it is indicated in the figure if other values were used. The NbSe₂ sample was capped with a thin Se layer to minimize oxidation during transport through air to prevent oxidation and was annealed twice to 250 °C to remove the Se-cap; the first anneal was sufficient to completely remove the Se cap, and topography images after first and second anneal were indistinguishable. No oxide was detected at the step edges [36] attesting to the efficiency of the capping and removal process. A third anneal was performed at 350 °C to test the material stability and resulted in the formation of numerous defects across the sample surface.

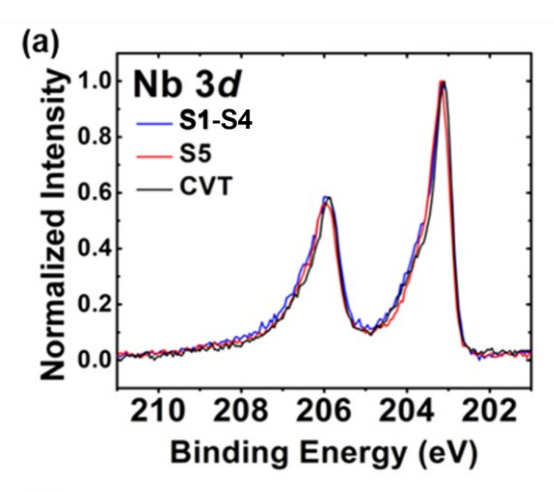
The topography images were leveled by mean plane leveling using Gwyddion [37]. Scanning tunneling spectroscopy (STS) was performed using point spectra, and so-called STS grid spectra. Grid spectra capture a complete topography image and for every third image pixel the feedback loop was opened and an I/V curve measured, followed by two pixels of topography imaging with a closed feedback loop. dI/dV curves were generated by numerical differentiation using a two-point method.

3. Results and Discussion

3.1 Characterization of NbSe₂ growth

Single crystal 2H-NbSe₂ flakes were grown using CVT as reference samples. 4-layer thick NbSe₂ were grown on SiO₂ by MBE. The growth of 4L NbSe₂ was characterized by insitu XPS. The core-level spectra of the Nb 3d and Se 3d core levels can be seen in Fig. 1 for S1-S4 on on 285 nm thick SiO₂/highly p-doped Si substrate and S5 on chemically grown SiO₂/intrinsic Si substrate. The lineshapes of the Nb 3d core level as observed in XPS of the MBE-grown 4L samples are consistent with the reference CVT-grown 2H-NbSe₂ (see Fig. 1). The Se 3d core level however differs from the expected lineshape of 2H-NbSe₂. This deviation of the Se 3d spectra is thought to be a consequence of intercalated Nb atoms which would change the coordination of adjacent Se

atoms. In contrast, the coordination of all Nb atoms is identical, thus the deviations in the Nb 3d spectra are subtle. The coordination of Nb and Se atoms in the Nb_{1+x}Se₂ structure has been discussed previously by Selte and Kjekshus [38]. photoelectron spectroscopy Angle-resolved (ARPES) measurements were carried out on MBE thin films grown on single-crystal graphene substrates using identical growth conditions to the samples discussed here (see Fig S9 in supplemental material, SM). No evidence of the expected dispersion associated with 1T-NbSe2 was found, suggesting that the chemical variability in these samples is not associated with the 1T phase of NbSe₂ [23,39]. The stoichiometry of the films in this work was determined to be Nb-rich when compared to our CVT reference sample with stoichiometries of samples S1 and S5 approximating NbSe_{1.93} (Nb_{1.04}Se₂) and NbSe_{1.91} (Nb_{1.05}Se₂), respectively. This value was calculated using the total measured Nb 3d and Se 3d areas from XPS



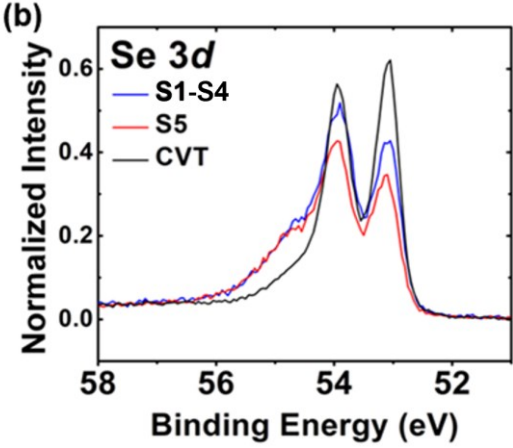


Fig. 1. (a) Nb 3*d* and (b) Se 3*d* core levels of NbSe₂ in samples S1-S4 (grown on 285 nm thick SiO₂/highly pdoped Si), S5 (grown on chemically grown SiO₂/intrinsic Si substrate) and a CVT grown reference sample. Spectra are normalized to the maximum Nb 3*d* intensity for each sample.

analysis and assuming a 2:1 Se to Nb stoichiometry for our CVT reference sample. X-ray diffraction of thicker MBE NbSe₂ samples grown under similar conditions suggest an expansion of the c-axis lattice parameter in our MBE grown films to 13.21 Å, ~5% increase when compared to our bulk CVT grown 2H-NbSe₂ crystal. The expanded lattice constant along the c-axis supports the theory of Nb-intercalation suggested by the stoichiometry calculations [40]. However, the nature of the chemical variability associated with these samples is not fully understood at this time and requires

further investigation. Full analysis of the XPS and APRES of these samples will be the focus of a future publication.

Figure 2a is a typical surface morphology for the NbSe₂ surface of S5 and is observed across the entire sample. It shows a relatively large corrugation and the islands are frequently fused, growing into one another rather than in a wedding cake type structure [41] often observed for TMDs. The island size is highly variable and is between 30 nm and 90 nm albeit the complex growth does not allow to properly assess the size distribution. Additionally, there are undulations

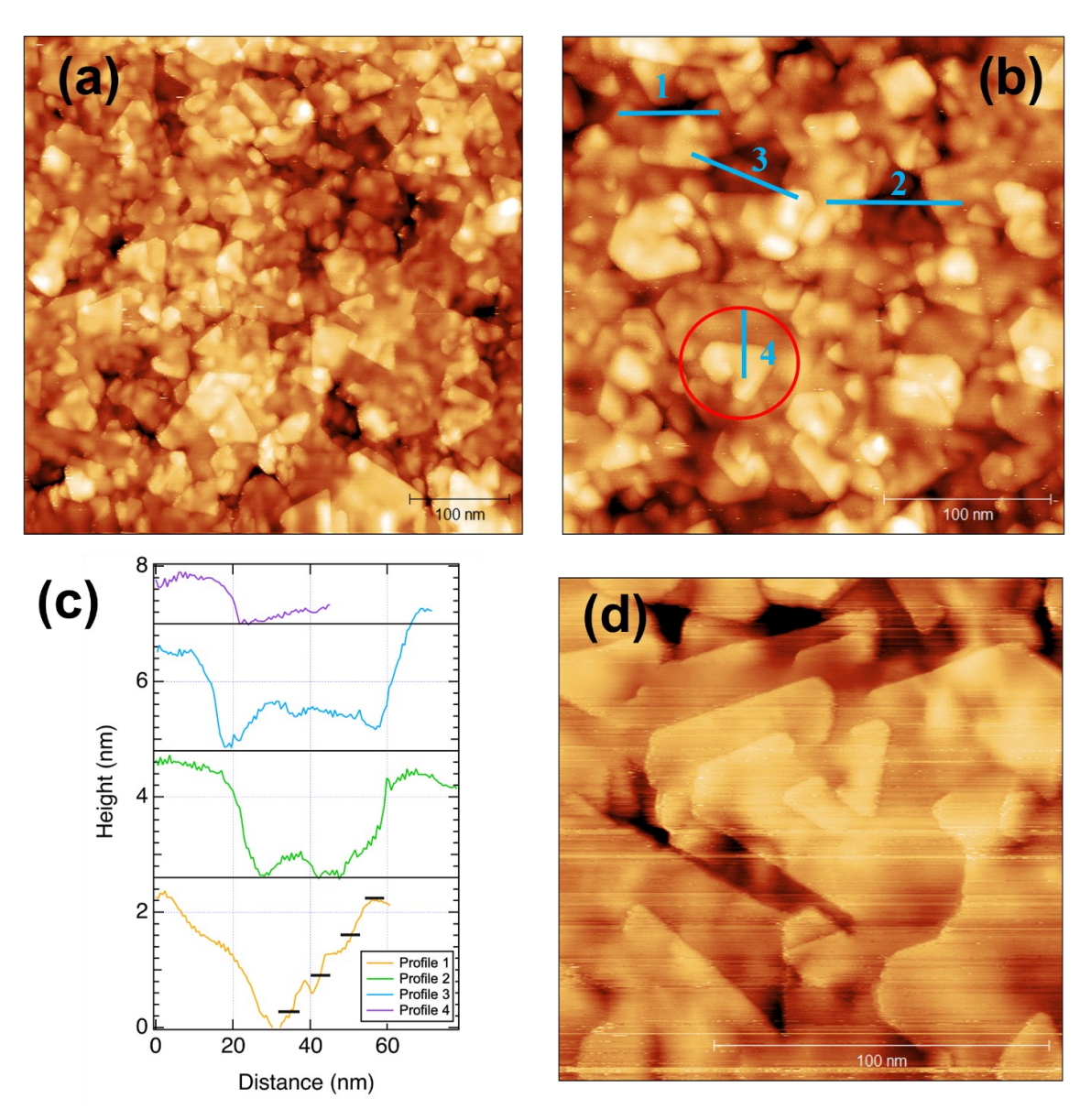
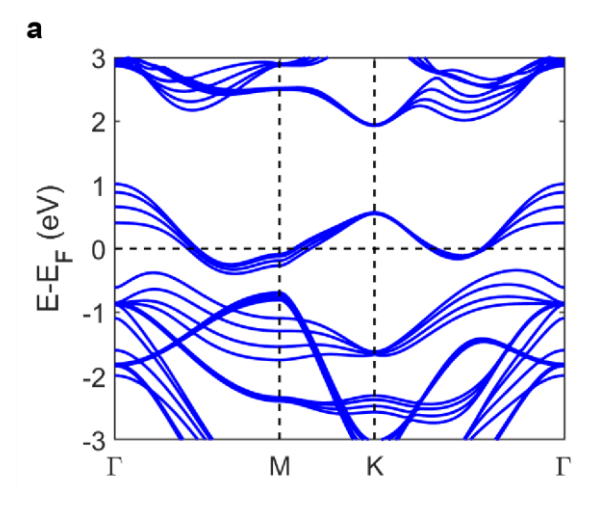


Fig. 2. Collection of representative topography images, which capture the layer structure, and growth mode of the NbSe₂ on chemically grown SiO₂/intrinsic Si sample. (a) Topography image with a size of 500 nm \times 500 nm image, and (b) shows a topography image covering 300 nm \times 300 nm imaged with $V_{bias} = -0.8$ V and $I_t = 0.2$ nA. The red circle indicates a screw dislocation, and the blue lines mark line scans summarized in (c). The height of a single NbSe₂ layer (0.62 nm) is indicated in profile 1 with black lines for guidance. The linescans are vertically offset for illustration. (d) is a topography image with a size of 150 nm \times 150 nm, which also includes a screw dislocation at the center of the image.



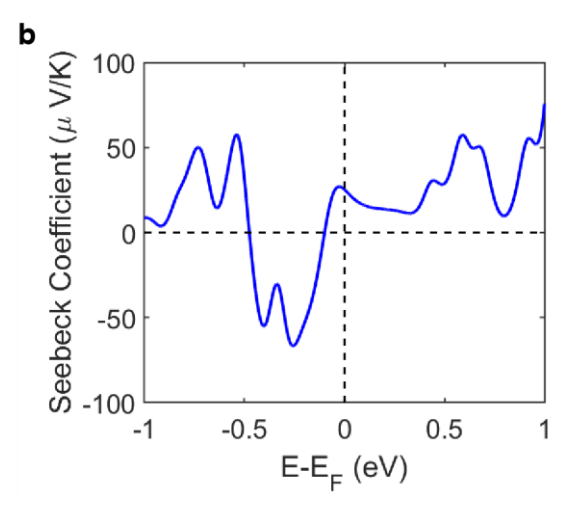


Fig. 3. (a) Band structure and (b) room temperature Seebeck coefficient versus the chemical potential for 4L-NbSe₂, calculated with DFT.

imprinted across all the layers, manifesting as brighter and darker patches within all islands independent of layer or size. The origin of these undulations is most likely related to inhomogeneities at the NbSe₂ – SiO₂ interface either in electronic structure or topography. The red circle in Fig. 2b highlights a screw dislocation [42], which is a feature found frequently across the entire sample surface. Figure 2d includes at the center of the image also a screw dislocation which involves several islands. Screw dislocations have been reported previously for MoS₂ [42] and are caused by the specific initial orientation of merging islands with competing growth fronts and located on different sides of a terraces step.

The blue lines in Fig. 2b mark the position of line scans as profiles of apparent height on the surface summarized in Fig. 2c. Profiles 1 and 2 are measured across the deepest depressions seen in the images to assess the number of layers. The depressions in profiles 1 and 2 capture the lowest-lying features in the images and are about 2.0 nm, which is commensurate with a stack of four NbSe₂ layers if the bottom of the profile is assumed to be the first layer, whereas a single layer of NbSe₂ has a height of 0.63 nm [43]. The islands with the largest apparent height, such as the one included on the right-hand edge of profile 3, might be the onset of the fifth layer. XPS and growth data support this assignment. Additional topography images of NbSe2 are included in the SM, and visualize the contribution of the exposed first layer, which is about 10 % of the surface area. Profile 4 shows an apparent height of about 0.8 nm commensurate with a single layer step. The corrugation of the layer surface and incomplete closure of the lower layers pose a significant challenge in the fabrication of few- or single-layer devices.

3.2 Electronic structure

We used density functional theory (DFT) to study the band structure of NbSe₂. The band structures of bulk and monolayer

2H-NbSe₂ have been discussed extensively in the literature [15,44,45]. The band structure of these two cases and their corresponding Seebeck coefficients are shown in the supplemental material. As shown in Fig. S5, both bulk and monolayer 2H-NbSe₂ are metallic with Fermi levels inside the band and a small Seebeck coefficient. As expected, in the case of a monolayer, the sample is overall less metallic as a result of the shift in the band levels. It is then anticipated that regardless of the number of layers, 2H-NbSe₂ preserves its metallic behavior.

Figure 3 shows the obtained band structure and the corresponding Seebeck coefficient for 4L-NbSe₂. The number of layers is set to four to represent the MBE grown samples accurately. The 4L-NbSe₂ remains metallic and the Fermi level (zero of the energy scale) is deep inside the band. Due to the metallic nature of the sample, the absolute Seebeck values are expected to be small. As shown in Fig. 3, our DFT calculations predict absolute values of less than 60 µV/K for chemical potentials smaller than 0.25 eV (relative to the intrinsic Fermi level) and less than 20 µV/K for intrinsic samples. The exact position of the chemical potential in our MBE-grown samples is not known, since the samples are Nb rich as discussed previously. The intercalation of the Nb atoms in between the layers [46] can result in a change in the chemical potential level and consequently a change in the Seebeck coefficient. Comparing the obtained results from DFT with measured room temperature Seebeck coefficient, we conclude that the chemical potential at room temperature is slightly less than 0.1 eV below the intrinsic Fermi level. We note that the measured Seebeck coefficients for both the CVT sample and MBE grown layers are negative at this temperature.

In the DFT calculations and within the reported Fermi window, the chemical potential stays within the same band. Although the chemical potential does not move to a different

band, the measured Seebeck changes sign, which is an indication that the slope of the density of states with respect to energy changes sign within the reported window. Since the samples are metallic, we can assume that the number of free carriers do not change with temperature. Our calculation shows that the carrier concentration of these samples is 4.3×10^{21} cm⁻³. Fixing the carrier concentration, we can calculate the Seebeck coefficient of the samples with respect to temperature. The calculated Seebeck coefficient values are shown in Fig. 4 and are in close agreement with the experimentally measured values. The slight differences could be associated with the constant relaxation approximation used in these calculations and slight changes in the carrier concentrations which were not included. Overall, the DFT results agree with the experiments, in terms of the values and the trend with respect to temperature.

The metallic nature of the samples is further confirmed using STM and measurements of the dI/dV, which is an indirect measure of the local density of states (LDOS). As shown in SM, dI/dV values are finite at various locations around the Fermi level. However, the lower islands (closer to the substrate) of the sample have smaller LDOS values compared to higher islands (closer to the top surface) and appear less metallic which is consistent with layer-dependent modifications of the LDOS.

Finally, the resistance of these samples cannot be obtained using constant relaxation time approximation. The relaxation times change significantly with temperature and while these changes do not affect the Seebeck coefficient, the resistance is inversely proportional to the mobility and is heavily influenced by the changes in the temperature. The major electron scattering for metals is due to acustic phonons. The electron-phonon scattering rate in this case increases linearly

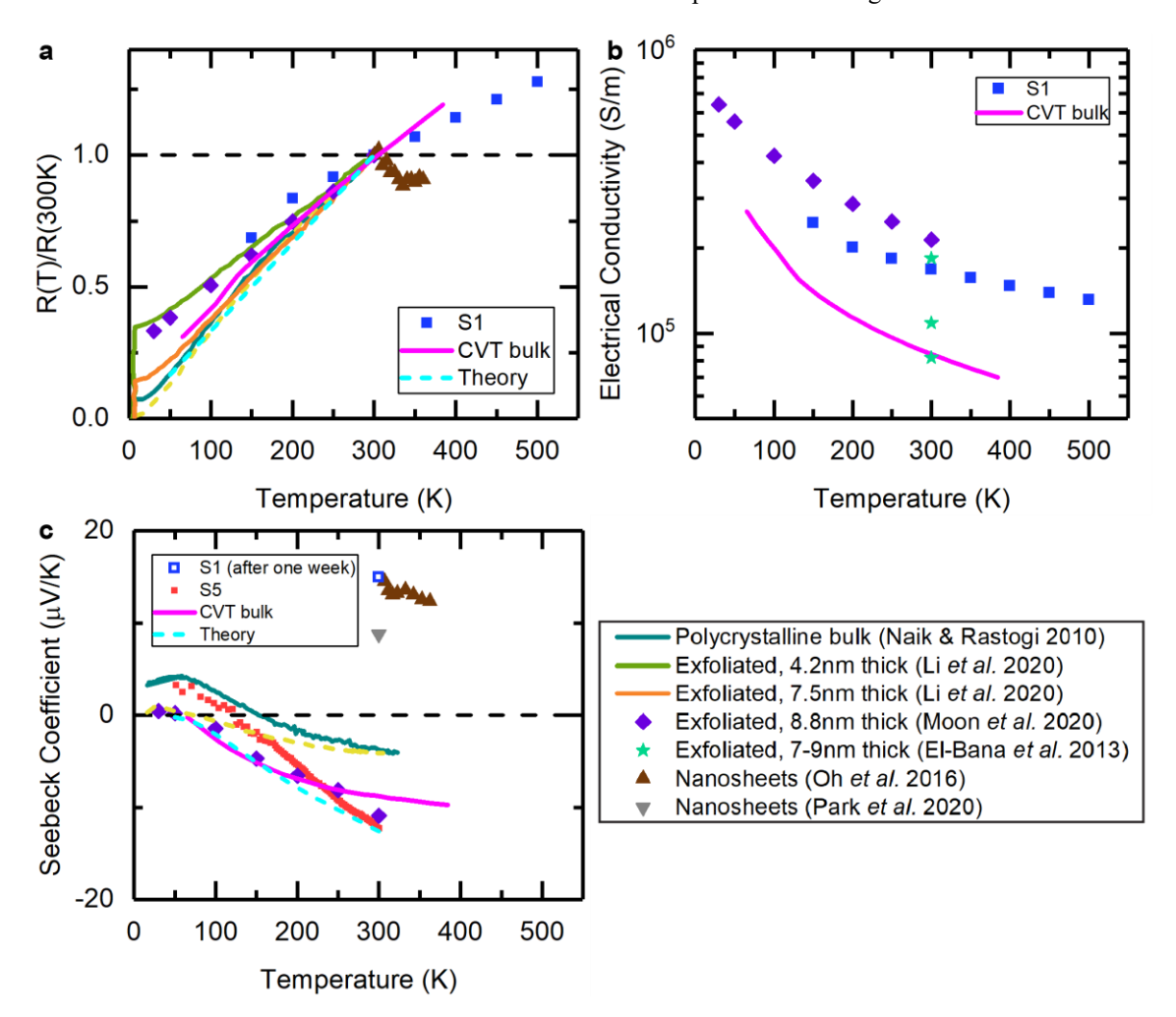


Fig. 4. Temperature-dependent electrical resistance and conductivity measurements, as well as Seebeck coefficient. (a) Normalized resistance of samples S1 and the CVT bulk reference sample, (b) electrical conductivity of S1 and the CVT sample, and (c) Seebeck coefficient of S1 (after one-week exposure to air) and S5, compared with the CVT sample, theoretical calculations and literature data [48–53]. Note that oxides were detected in the nanosheet samples and they were showing insulating behavior and a positive room temperature Seebeck coefficient [49,52].

with temperature, and can be modeled as $S_{e-ph} \propto g(E)$ [47], where g(E) is the density of states at energy E. Using this assumption and our privous assumption of constant carrier concentration with respect to the temperature, we can calculate the changes in the normalized resistance with respect to temperature. The results are shown in Fig. 4a and are in close agreement with experiment. In the next two sections, we discuss the experimental results in more details.

3.3 Normalized electrical resistance and electrical conductivity

The temperature dependence of the normalized four-point resistance, R(T)/R(300 K), is shown in Fig. 4a for device S1 and the CVT single crystal reference sample. S1 was fabricated from NbSe₂ film grown on 285 nm thick SiO₂/highly p-doped Si substrate, using photolithography and e-beam evaporation for electrodes. It had a thickness of 2.93 nm, corresponding to 4 layers estimated from XPS data. This device was measured inside a home-built JANIS cryostat system. The Se capping layer used to protect the samples in the atmosphere was removed at 500 K under vacuum ($\sim 10^{-6}$ Torr), prior to measurements. Detailed measurement configurations, raw data, and more devices (S2 and S3) can be found in Methods and SM.

Theoretical calculations for 4L-NbSe₂, literature data for bulk [48] and few-layer NbSe₂ samples [49–53] are plotted alongside data from this work for comparison in Fig. 4. The thin film sample S1 was measured from 150 K to 500 K, while the single crystal bulk sample was measured from 50 K to 400 K. The samples are purely metallic, and their resistances are an increasing function of temperature. Their rates of change with respect to temperature match well with theory and those from the literature (except the heavily oxidized nanosheet samples made by chemical exfoliation).

Fig. 4b shows the temperature-dependent electrical conductivity. At room temperature, S1 has a conductivity of around 1.68×10⁵ S/m, which is slightly smaller than that of the thicker exfoliated flake [50]. In comparison, the CVT single crystal sample has an electrical conductivity that is about half of that value.

The electrical properties of NbSe₂ are highly sensitive to the growth method, to the device fabrication protocols and to the ambient conditions. As illustrated in the case of the 7-9 nm thick exfoliated flakes [53], even when they were fabricated following the same procedures, their room temperature conductivity varied from 8.2×10⁴ to 1.8×10⁵ S/m. The electrical conductivities of S1 and the CVT sample are within the range of the reported values. In order to better understand the samples, we performed Hall measurements on the CVT bulk sample. Its Hall carrier concentration was measured to be around 4.1×10²¹ cm⁻³ at room temperature, which is very close to the theoretically estimated value of the 4L sample. The exfoliated flakes reported in literatures [50,53] were made

from high quality single crystals and thus we assume they had a high structural quality similar to the CVT sample and a similar carrier concentration. The main difference between the samples is most likely their mobility. Bulk and few layer NbSe₂ are reported to have room temperature mobility in the range of $0.5 - 3 \text{ cm}^2/\text{V} \cdot \text{s}$ [54,55] and there is no clear thickness dependence. The Hall mobility of the CVT sample was calculated as 1.7 cm²/V·s, within this reported range. The 8.8 nm thick flake [50] is expected to have a high mobility of close to 3 cm²/V·s based on its high electrical conductivity. Although S1 is comprised of many islands, it shows higher mobility than the CVT single crystal. The carrier mean free path in 4L NbSe₂ was estimated to be about 20 nm at 50 K limited by the thickness [56], and should drop significantly at higher temperatures due to electron-phonon scattering. In comparison, the islands of S1 are between 30 and 90 nm in size. Their impact on carrier mobility is minimal and the mobility of S1 remains high.

3.4 Seebeck coefficient

The temperature dependent Seebeck coefficient for device S5 and room temperature value for S1 (which was exposed to air for one week after electrical conductivity measurements) are presented in Fig. 4c, together with the CVT reference. Device S5 was fabricated from NbSe₂ grown on a few-nmthick chemically grown SiO₂/intrinsic Si substrate and gold-copper electrodes were attached to the sides of the sample for measurements inside a commercial VERSALAB system. Its Se capping layer was removed at 400 K under vacuum before measurements.

The Seebeck coefficient of S5 starts from around $-12~\mu\text{V/K}$ at room temperature, gradually increases as the temperature goes down, eventually crosses over to a positive value around 120 K, and continues to increase to about $+3~\mu\text{V/K}$ at 50 K. The values and the overall trend agree well with the CVT bulk sample, as well as reference data for 2H bulk and exfoliated thin flake samples [48,50]. For single-crystal samples, whether as a bulk crystal or as a few-nm thick exfoliate flake, the negative-to-positive crossover temperature is around 50 K [48,50]. However, this temperature increases to about 120 K for the polycrystalline thin film S5 and about 150 K for the referenced polycrystalline bulk sample [48]. The grain sizes and boundaries might have some effect on this crossover temperature, which could be of value for further investigation.

The theoretical Seebeck coefficient of 4L-NbSe₂ follows a similar trend and approaches zero as the temperature goes to 50 K. The behavior matches the single crystal data well, since a perfect crystal has been assumed in the calculations. This provides further evidence to our speculation that grain boundaries can modulate the Seebeck cross-over temperature.

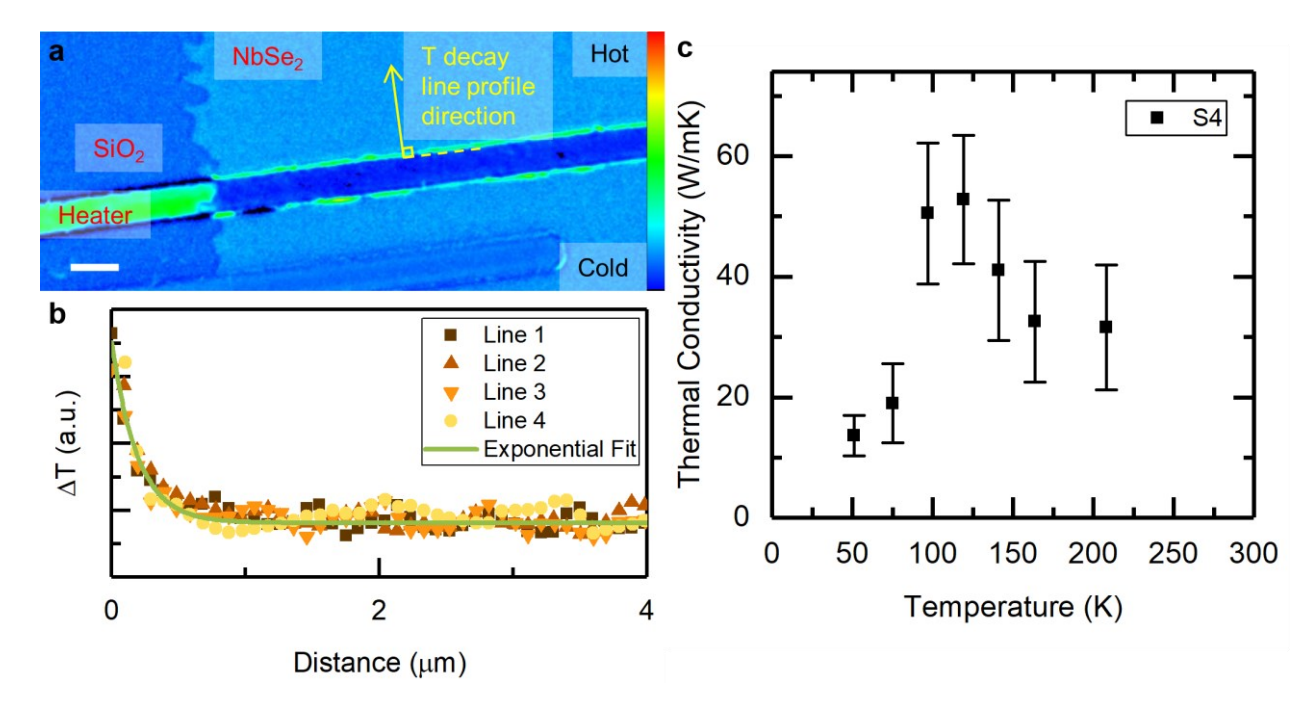


Fig. 5. (a) Example temperature map at 50 K, (b) example temperature decay curves taken from (a) and their corresponding exponential fitting curve, and (c) temperature-dependent in-plane thermal conductivity from 50 K to 210 K for device S4. The scale bar in (a) is 5 µm. The same thermoreflectance coefficient is assumed for the entire sample surface, since only how the temperature decays with distance affects the extracted thermal conductivity, not the absolute temperature values.

It is interesting to note that a positive room temperature value of around +15 μV/K was obtained for S1 after being exposed to air (kept in a desiccator after Se cap removal) for roughly a week, while the S5 sample, which was not exposed, has a negative Seebeck coefficient at room temperature. The observed positive Seebeck coefficient matches the reported values for NbSe₂ nanosheet samples [49,52], in which the existence of oxide Nb₂O₅ has been confirmed by XPS measurements. Although the exact oxide content of S1 at the time of the measurement was not known, its resistance was orders of magnitude higher than before and other samples (S2 and S3 in SM) measured in the same week showed insulating behavior. The temperature-dependent normalized resistance of S3 matches that of the oxidized nanosheet [49] above room temperature. Oxidation seems to be a major factor leading to these positive values.

3.5 Thermal conductivity

The thermal conductivity of device S4 (fabricated in the same batch as S1) was measured using heat diffusion imaging method [28] at low temperatures. Heat diffusion imaging is an electrical-pump optical-probe method based on the thermoreflectance technique. In-plane thermal conductivity of a supported thin film is extracted by fitting the temperature decay in the longitudinal direction to an exponential function according to the heat spreader model. The detailed data analysis is included in SM.

As shown in Fig. 5, the thermal conductivity rises to a maximum of about (53 ± 11) W/m·K as the temperature increases from 50 K to 120 K, then gradually decreases and almost reaches a plateau of $(32 \pm 10) \text{ W/m·K}$ as the temperature gets closer to room temperature at 200 K. Although the sample was metallic, Wiedemann-Franz law estimated the electronic thermal conductivity to be about 1.5 W/mK at 200 K, comprising less than 5% of the total value. The thermal transport was dominated by phonons. More phonon-phonon scattering is expected with increasing temperature and therefore leads to shorter temperature decay length. Our measurement at higher temperatures was limited by optical resolution. This increasing then decreasing trend in thermal conductivity with respect to increasing temperature resembles that in a previous report on bulk NbSe₂ [57], although the maxima occur at different temperatures and the overall thermal conductivity is surprisingly larger than the bulk equivalent. The largest thermal conductivity is reached at 120 K for the 4L Nb_{1+x}Se₂. In another few-layer TMD, 4L-MoS₂, the largest thermal conductivity also occurs at around 120K, where the behavior below 120 K is attributed to phonon-boundary scattering and that above 120 K is attributed to phonon-phonon scattering [58]. To the best of our knowledge, this is the first in-plane thermal conductivity measurement of few-layer NbSe₂ samples in this temperature range. However, a room temperature value of (15 \pm 4) W/m·K for exfoliated 2H-NbSe₂ flakes (about 20 nm to 25 nm thick)

using the Raman method was reported in a recent master's thesis [59].

3.6 Power factor, PF, and thermoelectric figure of merit, zT

A discussion on the two parameters used to characterize a material's thermoelectric performance, $PF (\sigma S^2)$ and zT $(\sigma S^2 T/k)$, is called for since the temperature-dependent measurements of their constituents, i.e., electrical conductivity σ , Seebeck coefficient S and thermal conductivity k, have been performed. Although a thermal conductivity value could not be obtained at room temperature, PF and zTvalues of the few-layer samples are expected to be small due to the small Seebeck value (about $-12.3 \,\mu\text{V/K}$). The room temperature PF is slightly smaller than that of the oxidized NbSe₂ nanosheets reported by Oh et al. [49]; but is 3 times as high as that from Park et al. [52] and 4 times that of the CVT reference sample. If we take the thermal conductivity value at 200 K as the room temperature value, zT is estimated to be on the order of 10⁻⁴. As temperature decreases, although the electrical conductivity gets higher, the absolute Seebeck coefficient becomes too close to zero to yield better PF or zT.

4. Conclusion

In summary, we have demonstrated the growth of few-layer NbSe₂ by MBE on SiO₂. Using In-situ XPS we showed these thin films are Nb-rich Nb_{1+x}Se₂. The extra Nb atoms are possibly intercalated between the layers resulting in a larger separation of the layers. The STM has confirmed the metallic nature of the samples, however, it also shows that the samples were inhomogeneous and had lower LDOS closer to the substrate. The metallic nature of the four layer sample was also confirmed with DFT calculations. Theoretical Seebeck coefficients as well as the normalized resistance were calculated with respect to temperature, and agreed well with experiments.

Several devices were fabricated from full-coverage NbSe₂ thin films for measurements of their in-plane thermoelectric properties across a wide temperature range. It was observed that exposure to air and oxidization changed the Seebeck coefficient from a small negative number to a positive number with a larger absolute value. However, it resulted in a significant drop in electrical conductivity. The Seebeck coefficient of the few-layer NbSe₂ (prior to oxidization) had a very similar trend as that of the single crystal CVT sample. However, the transition temperature wherein the sign of the Seebeck changes was different. Despite the Se deficiency and the many islands which introduce extra scattering, the MBEgrown samples show higher electrical and thermal conductivity values compared to single-crystal 2H bulk samples. While the larger electrical conductivity could be attributed to larger carrier concentrations, it is difficult to explain the larger thermal conductivity and the latter should be the subject of future investigations. These measurements open up dialogues about the transport properties of few-layer NbSe₂ and should be considered a step towards the optimization of NbSe₂ for device applications.

Supplemental material

The following information is included in supplemental material: device configuration for transport measurement, the electrical conductivity of S2 and S3, details of thermal conductivity analysis, scanning tunneling spectroscopy analysis, and angle-resolved photoelectron spectroscopy of MBE grown NbSe₂.

Author Contributions

M.Z and S.J.M. designed and supervised the research. P.L. synthesized the MBE samples. S.K. and A.V.D. grew the NbSe₂ samples using CVT method. T.Z. fabricated the devices and performed the thermoelectric transport measurements. M.G.R. performed the DFT calculations. M.S.A. contributed to measurements using VERSALAB. F.F.T. contributed to thermal conductivity measurement. D.J. and P.R. performed and analyzed the STM measurements. The manuscript was drafted by T.Z. and M.Z. and completed through the contributions of all authors. All authors have approved the final version of the manuscript.

Acknowledgement

T.Z. and M.Z. acknowledge the NSF grant number 1653268. M.G.R acknowledges the UVA's Rivanna cluster which was used for the calculations. S. K. and A. V. D. acknowledge support through the Materials Genome Initiative funding allocated to the National Institute of Standards and Technology. D.J. and P.R acknowledge the support by NSF-DMR Metals and Metallic Nanosctructures award number 2004326.

Disclaimer

Certain commercial equipment, instruments, or materials are identified in this paper in order to specify the experimental procedure adequately. Such identification is not intended to imply recommendation or endorsement by the National Institute of Standards and Technology, nor is it intended to imply that the materials or equipment identified are necessarily the best available for the purpose.

Data availability

The data that support the findings of this study are available from the corresponding authors upon reasonable request.

References

- [1] E. Scalise, M. Houssa, G. Pourtois, V. Afanas'ev, A. Stesmans, Strain-induced semiconductor to metal transition in the two-dimensional honeycomb structure of MoS2, Nano Res. 5 (2012) 43–48. https://doi.org/10.1007/s12274-011-0183-0.
- [2] S. Nayeb Sadeghi, M. Zebarjadi, K. Esfarjani, Biaxial tensile strain-induced enhancement of thermoelectric performance of TiSe2 monolayer based on first-principles calculation, J. Mater. Chem. C. (2019). https://doi.org/10.1039/C9TC00183B.
- [3] A. Ramasubramaniam, D. Naveh, E. Towe, Tunable band gaps in bilayer transition-metal dichalcogenides, Phys. Rev. B. 84 (2011) 205325. https://doi.org/10.1103/PhysRevB.84.205325.
- [4] K.F. Mak, C. Lee, J. Hone, J. Shan, T.F. Heinz, Atomically Thin MoS2: A New Direct-Gap Semiconductor, Phys. Rev. Lett. 105 (2010) 136805. https://doi.org/10.1103/PhysRevLett.105.136805.
- [5] A. Kuc, N. Zibouche, T. Heine, Influence of quantum confinement on the electronic structure of the transition metal sulfide TS2, Phys. Rev. B. 83 (2011) 245213. https://doi.org/10.1103/PhysRevB.83.245213.
- [6] S. Manzeli, D. Ovchinnikov, D. Pasquier, O. V. Yazyev, A. Kis, 2D transition metal dichalcogenides, Nat. Rev. Mater. 2 (2017) 17033. https://doi.org/10.1038/natrevmats.2017.33.
- [7] Q. Li, Q. Hao, T. Zhu, M. Zebarjadi, K. Takahashi, Nanostructured and Heterostructured 2D Materials for Thermoelectrics, Eng. Sci. 13 (2020) 24–50. https://doi.org/10.30919/es8d1136.
- [8] A. Ziabari, M. Zebarjadi, D. Vashaee, A. Shakouri, Nanoscale solid-state cooling: a review, Reports Prog. Phys. 79 (2016) 095901. https://doi.org/10.1088/0034-4885/79/9/095901.
- [9] J. Duan, X. Wang, X. Lai, G. Li, K. Watanabe, T. Taniguchi, M. Zebarjadi, E.Y. Andrei, High thermoelectricpower factor in graphene/hBN devices, Proc. Natl. Acad. Sci. 113 (2016) 14272–14276. https://doi.org/10.1073/pnas.1615913113.
- [10] J. Wu, Y.Y. Liu, Y.Y. Liu, Y. Cai, Y. Zhao, H.K. Ng, K. Watanabe, T. Taniguchi, G. Zhang, C.-W. Qiu, D. Chi, A.H.C. Neto, J.T.L. Thong, K.P. Loh, K. Hippalgaonkar, Large enhancement of thermoelectric performance in MoS 2 / h -BN heterostructure due to vacancy-induced band hybridization, Proc. Natl. Acad. Sci. 117 (2020) 13929–13936. https://doi.org/10.1073/pnas.2007495117.
- [11] X. Xi, L. Zhao, Z. Wang, H. Berger, L. Forró, J. Shan, K.F. Mak, Strongly enhanced charge-density-wave order in monolayer NbSe2, Nat. Nanotechnol. 10 (2015) 765–769. https://doi.org/10.1038/nnano.2015.143.
- X. Xi, Z. Wang, W. Zhao, J.-H. Park, K.T. Law, H. Berger,
 L. Forró, J. Shan, K.F. Mak, Ising pairing in superconducting NbSe2 atomic layers, Nat. Phys. 12 (2016) 139–143. https://doi.org/10.1038/nphys3538.
- [13] M.M. Ugeda, A.J. Bradley, Y. Zhang, S. Onishi, Y. Chen, W. Ruan, C. Ojeda-Aristizabal, H. Ryu, M.T. Edmonds, H.-Z. Tsai, A. Riss, S.-K. Mo, D. Lee, A. Zettl, Z. Hussain, Z.-X. Shen, M.F. Crommie, Characterization of collective ground states in single-layer NbSe2, Nat. Phys. 12 (2016) 92–97. https://doi.org/10.1038/nphys3527.
- [14] U. Chatterjee, J. Zhao, M. Iavarone, R. Di Capua, J.P. Castellan, G. Karapetrov, C.D. Malliakas, M.G. Kanatzidis, H. Claus, J.P.C. Ruff, F. Weber, J. van Wezel, J.C. Campuzano, R. Osborn, M. Randeria, N. Trivedi,

- M.R. Norman, S. Rosenkranz, Emergence of coherence in the charge-density wave state of 2H-NbSe2, Nat. Commun. 6 (2015) 6313. https://doi.org/10.1038/ncomms7313.
- [15] J.Á. Silva-Guillén, P. Ordejón, F. Guinea, E. Canadell, Electronic structure of 2H-NbSe2 single-layers in the CDW state, 2D Mater. 3 (2016) 035028. https://doi.org/10.1088/2053-1583/3/3/035028.
- [16] L.B. Lei, C. Zhang, A.B. Yu, Y.F. Wu, W. Peng, H. Xiao, S. Qiao, T. Hu, The transport properties of ultrathin 2H-NbSe 2, Supercond. Sci. Technol. Supercond. Sci. Technol. 34 (2021) 5. https://doi.org/10.1088/1361-6668/abd14f.
- [17] A. Hamill, B. Heischmidt, E. Sohn, D. Shaffer, K.-T. Tsai, X. Zhang, X. Xi, A. Suslov, H. Berger, L. Forró, F.J. Burnell, J. Shan, K.F. Mak, R.M. Fernandes, K. Wang, V.S. Pribiag, Two-fold symmetric superconductivity in few-layer NbSe2, Nat. Phys. 17 (2021) 949–954. https://doi.org/10.1038/s41567-021-01219-x.
- [18] E. Zhang, X. Xu, Y.-C. Zou, L. Ai, X. Dong, C. Huang, P. Leng, S. Liu, Y. Zhang, Z. Jia, X. Peng, M. Zhao, Y. Yang, Z. Li, H. Guo, S.J. Haigh, N. Nagaosa, J. Shen, F. Xiu, Nonreciprocal superconducting NbSe2 antenna, Nat. Commun. 11 (2020) 5634. https://doi.org/10.1038/s41467-020-19459-5.
- [19] F. Kadijk, F. Jellinek, On the polymorphism of niobium diselenide, J. Less Common Met. 23 (1971) 437–441. https://doi.org/10.1016/0022-5088(71)90053-1.
- [20] F. Bischoff, W. Auwärter, J. V Barth, A. Schiffrin, M. Fuhrer, B. Weber, Nanoscale Phase Engineering of Niobium Diselenide, Chem. Mater. 29 (2017) 9907–9914. https://doi.org/10.1021/acs.chemmater.7b03061.
- [21] H. Wang, J. Lee, M. Dreyer, B.I. Barker, A scanning tunneling microscopy study of a new superstructure around defects created by tip–sample interaction on 2H- NbSe 2, J. Phys. Condens. Matter. 21 (2009) 265005. https://doi.org/10.1088/0953-8984/21/26/265005.
- [22] N. Ramšak, H.J.P. van Midden, A. Prodan, V. Marinković, F.W. Boswell, J.C. Bennett, Defect-induced roomtemperature modulation in NbSe2, Phys. Rev. B. 60 (1999) 4513–4516. https://doi.org/10.1103/PhysRevB.60.4513.
- [23] Y. Nakata, K. Sugawara, R. Shimizu, Y. Okada, P. Han, T. Hitosugi, K. Ueno, T. Sato, T. Takahashi, Monolayer 1T-NbSe2 as a Mott insulator, NPG Asia Mater. 8 (2016) e321–e321. https://doi.org/10.1038/am.2016.157.
- [24] L. Liu, H. Yang, Y. Huang, X. Song, Q. Zhang, Z. Huang, Y. Hou, Y. Chen, Z. Xu, T. Zhang, X. Wu, J. Sun, Y. Huang, F. Zheng, X. Li, Y. Yao, H.-J. Gao, Y. Wang, Direct identification of Mott Hubbard band pattern beyond charge density wave superlattice in monolayer 1T-NbSe2, Nat. Commun. 12 (2021) 1978. https://doi.org/10.1038/s41467-021-22233-w.
- [25] Z. Liu, J. Wang, B. Chen, Y. Wei, W. Liu, J. Liu, Giant Enhancement of Continuous Wave Second Harmonic Generation from Few-Layer GaSe Coupled to High- Q Quasi Bound States in the Continuum, Nano Lett. 21 (2021) 7405–7410. https://doi.org/10.1021/ACS.NANOLETT.1C01975/SUPP L FILE/NL1C01975 SI 001.PDF.
- [26] M. Liu, J. Leveillee, S. Lu, J. Yu, H. Kim, C. Tian, Y. Shi, K. Lai, C. Zhang, F. Giustino, C.-K. Shih, Monolayer 1T-NbSe 2 as a 2D-correlated magnetic insulator, Sci. Adv. 7 (2021) 6339. https://doi.org/10.1126/sciadv.abi6339.
- [27] K.M. Freedy, P.M. Litwin, S.J. McDonnell, (Invited) In-Vacuo Studies of Transition Metal Dichalcogenide

- Synthesis and Layered Material Integration, ECS Trans. 77 (2017) 11–25. https://doi.org/10.1149/07708.0011ecst.
- [28] T. Zhu, D.H. Olson, P.E. Hopkins, M. Zebarjadi, Heat diffusion imaging: In-plane thermal conductivity measurement of thin films in a broad temperature range, Rev. Sci. Instrum. 91 (2020) 113701. https://doi.org/10.1063/5.0024476.
- [29] P. Giannozzi, S. Baroni, N. Bonini, M. Calandra, R. Car, C. Cavazzoni, D. Ceresoli, G.L. Chiarotti, M. Cococcioni, I. Dabo, A. Dal Corso, S. de Gironcoli, S. Fabris, G. Fratesi, R. Gebauer, U. Gerstmann, C. Gougoussis, A. Kokalj, M. Lazzeri, L. Martin-Samos, N. Marzari, F. Mauri, R. Mazzarello, S. Paolini, A. Pasquarello, L. Paulatto, C. Sbraccia, S. Scandolo, G. Sclauzero, A.P. Seitsonen, A. Smogunov, P. Umari, R.M. Wentzcovitch, QUANTUM ESPRESSO: a modular and open-source software project for quantum simulations of materials, J. Phys. Condens. Matter. 21 (2009) 395502. https://doi.org/10.1088/0953-8984/21/39/395502.
- [30] J.P. Perdew, A. Ruzsinszky, G.I. Csonka, O.A. Vydrov, G.E. Scuseria, L.A. Constantin, X. Zhou, K. Burke, Restoring the Density-Gradient Expansion for Exchange in Solids and Surfaces, Phys. Rev. Lett. 100 (2008) 136406. https://doi.org/10.1103/PhysRevLett.100.136406.
- [31] P.E. Blöchl, C.J. Först, J. Schimpl, Projector augmented wave method:ab initio molecular dynamics with full wave functions, Bull. Mater. Sci. 26 (2003) 33–41. https://doi.org/10.1007/BF02712785.
- [32] M. Born, R. Oppenheimer, Zur Quantentheorie der Molekeln, Ann. Phys. 389 (1927) 457–484. https://doi.org/10.1002/andp.19273892002.
- [33] R. Fletcher, Practical Methods of Optimization, John Wiley & Sons, Ltd, Chichester, West Sussex England, West Sussex England, 2000. https://doi.org/10.1002/9781118723203.
- [34] G.K.H. Madsen, D.J. Singh, BoltzTraP. A code for calculating band-structure dependent quantities, Comput. Phys. Commun. 175 (2006) 67–71. https://doi.org/10.1016/j.cpc.2006.03.007.
- [35] B.R. Nag, Electron Transport in Compound Semiconductors, Springer-Verlag, Berlin, 1980.
- [36] R. Addou, C.M. Smyth, J.-Y. Noh, Y.-C. Lin, Y. Pan, S.M. Eichfeld, S. Fölsch, J.A. Robinson, K. Cho, R.M. Feenstra, R.M. Wallace, One dimensional metallic edges in atomically thin WSe2 induced by air exposure, 2D Mater. 5 (2018) 025017. https://doi.org/10.1088/2053-1583/AAB0CD.
- [37] D. Nečas, P. Klapetek, Gwyddion: an open-source software for SPM data analysis, Open Phys. 10 (2012) 181–188. https://doi.org/10.2478/s11534-011-0096-2.
- [38] K. Selte, A. Kjekshus, B. Thorkilsen, H. Halvarson, L. Nilsson, On the Structural Properties of the Nb(1+x)Se2 Phase., Acta Chem. Scand. 18 (1964) 697–706. https://doi.org/10.3891/acta.chem.scand.18-0697.
- [39] Y. Nakata, K. Sugawara, A. Chainani, H. Oka, C. Bao, S. Zhou, P.-Y. Chuang, C.-M. Cheng, T. Kawakami, Y. Saruta, T. Fukumura, S. Zhou, T. Takahashi, T. Sato, Robust charge-density wave strengthened by electron correlations in monolayer 1T-TaSe2 and 1T-NbSe2, Nat. Commun. 12 (2021) 5873. https://doi.org/10.1038/s41467-021-26105-1.
- [40] R. Huisman, F. Kadijk, F. Jellinek, The non-stoichiometric phases Nb1+xSe2 and Ta1+xSe2, J. Less Common Met. 21 (1970) 187–193. https://doi.org/10.1016/0022-

- 5088(70)90117-7.
- [41] A. Costine, P. Delsa, T. Li, P. Reinke, P. V. Balachandran, Data-driven assessment of chemical vapor deposition grown MoS 2 monolayer thin films, J. Appl. Phys. 128 (2020) 235303. https://doi.org/10.1063/5.0017507.
- [42] X. Dong, C. Yan, D. Tomer, C.H. Li, L. Li, Spiral growth of few-layer MoS 2 by chemical vapor deposition, Appl. Phys. Lett. 109 (2016) 051604. https://doi.org/10.1063/1.4960583.
- [43] R.F. Frindt, Superconductivity in Ultrathin NbSe2 Layers, Phys. Rev. Lett. 28 (1972) 299–301. https://doi.org/10.1103/PhysRevLett.28.299.
- [44] W.-Y. He, B.T. Zhou, J.J. He, N.F.Q. Yuan, T. Zhang, K.T. Law, Magnetic field driven nodal topological superconductivity in monolayer transition metal dichalcogenides, Commun. Phys. 1 (2018) 40. https://doi.org/10.1038/s42005-018-0041-4.
- [45] L.F. Mattheiss, Band Structures of Transition-Metal-Dichalcogenide Layer Compounds, Phys. Rev. B. 8 (1973) 3719–3740. https://doi.org/10.1103/PhysRevB.8.3719.
- [46] K. Selte, E. Bjerkelund, A. Kjekshus, Intermediate phases in the systems niobium-selenium, niobium-tellurium, tantalum-selenium, and tantalum-tellurium, J. Less Common Met. 11 (1966) 14–30. https://doi.org/10.1016/0022-5088(66)90053-1.
- [47] M. Lundstrom, Fundamentals of Carrier Transport, Cambridge University Press, 2000. https://doi.org/10.1017/CBO9780511618611.
- I. Naik, A.K. Rastogi, Transport properties of 2H-NbSe2:
 Effect of Ga-intercalation, Phys. B Condens. Matter. 405 (2010) 955–957.
 https://doi.org/10.1016/j.physb.2009.10.028.
- [49] J.Y. Oh, J.H. Lee, S.W. Han, S.S. Chae, E.J. Bae, Y.H. Kang, W.J. Choi, S.Y. Cho, J.-O. Lee, H.K. Baik, T. Il Lee, Chemically exfoliated transition metal dichalcogenide nanosheet-based wearable thermoelectric generators, Energy Environ. Sci. 9 (2016) 1696–1705. https://doi.org/10.1039/C5EE03813H.
- [50] H. Moon, J. Kim, J. Bang, S. Hong, S. Youn, H. Shin, J.W. Roh, W. Shim, W. Lee, Semimetallic features in thermoelectric transport properties of 2H–3R phase niobium diselenide, Nano Energy. 78 (2020) 105197. https://doi.org/10.1016/j.nanoen.2020.105197.
- [51] X.-Q. Li, Z.-L. Li, J.-J. Zhao, X.-S. Wu, Electrical and thermoelectric study of two-dimensional crystal of NbSe2, Chinese Phys. B. 29 (2020) 087402. https://doi.org/10.1088/1674-1056/ab9614.
- [52] H. Park, J.Y. Kim, J.Y. Oh, T. Il Lee, Long-term stable NbSe2 nanosheet aqueous ink for printable electronics, Appl. Surf. Sci. 504 (2020) 144342. https://doi.org/10.1016/j.apsusc.2019.144342.
- [53] M.S. El-Bana, D. Wolverson, S. Russo, G. Balakrishnan, D.M. Paul, S.J. Bending, Superconductivity in twodimensional NbSe2 field effect transistors, Supercond. Sci. Technol. 26 (2013) 125020. https://doi.org/10.1088/0953-2048/26/12/125020.
- [54] H.N.S. Lee, H. McKinzie, D.S. Tannhauser, A. Wold, The Low-Temperature Transport Properties of NbSe 2, J. Appl. Phys. 40 (1969) 602–604. https://doi.org/10.1063/1.1657440.
- [55] K.S. Novoselov, D. Jiang, F. Schedin, T.J. Booth, V. V Khotkevich, S. V Morozov, A.K. Geim, Two-dimensional atomic crystals, Proc. Natl. Acad. Sci. 102 (2005) 10451– 10453. https://doi.org/10.1073/pnas.0502848102.

- [56] E. Khestanova, J. Birkbeck, M. Zhu, Y. Cao, G.L. Yu, D. Ghazaryan, J. Yin, H. Berger, L. Forró, T. Taniguchi, K. Watanabe, R. V. Gorbachev, A. Mishchenko, A.K. Geim, I. V. Grigorieva, Unusual Suppression of the Superconducting Energy Gap and Critical Temperature in Atomically Thin NbSe2, Nano Lett. 18 (2018) 2623–2629. https://doi.org/10.1021/acs.nanolett.8b00443.
- [57] V.I. Beletskii, O.A. Gavrenko, B.A. Merisov, M.A. Obolenskii, A. V. Sologubenko, G.Y. Khadjai, K.B. Chashka, Thermal conductivity and electrical resistivity of the layered compound Nb1-xSnxSe2, Low Temp. Phys. 24 (1998) 273–277. https://doi.org/10.1063/1.593583.
- [58] I. Jo, M.T. Pettes, E. Ou, W. Wu, L. Shi, Basal-plane thermal conductivity of few-layer molybdenum disulfide, Appl. Phys. Lett. 104 (2014) 201902. https://doi.org/10.1063/1.4876965.
- [59] H.-H. Lien, THERMAL CONDUCTIVITY OF THIN FILM NIOBIUM DISELENIDE FROM TEMPERATURE-DEPENDENT RAMAN, 2017.